A pairwise/sandwich-like assembly consisting of a TaO_3 nanomesh and reduced graphene oxide for a pelletized self-supported cathode towards high-areal-capacity Li–S batteries

Chenhui Wang, Nobuyuki Sakai,* Yasuo Ebina, Shigeru Suehara, Takayuki Kikuchi, Daiming Tang, Renzhi Ma and Takayoshi Sasaki*

International Center for Materials Nanoarchitectonics (WPI-MANA), National Institute for Materials Science (NIMS), Namiki 1-1, Tsukuba, Ibaraki 305-0044, Japan.
E-mail: sasaki.takayoshi@nims.go.jp; sakai.nobuyuki@nims.go.jp

Lithium-sulfur (Li-S) batteries have attracted considerable attention as a promising energy storage technology. However, the low loading and utilization of sulfur result in the poor practical energy density of these batteries, which has hindered their extensive application. Herein, we demonstrate the fabrication of a molecular pairwise/sandwich-like assembly of TaO_3/rGO, which can be pelletized into a self-supported cathode to improve sulfur loading and utilization. This unique pairwise/sandwich-like heterostructure of TaO_3/rGO was produced through a solution process via self-assembly and identified by X-ray diffraction analysis/simulation and TEM observations. The molecular-scale heterostructure maximizes attractive features of the TaO_3 nanomesh: crystalline open channels, polar Ta-O bonds, Lewis acid surfaces and largely exposed active sites, by combining with electrically conductive rGO. As a result, the heterostructure exhibited fast Li^+ transfer, effective confinement of polysulfides and high catalytic activity for the conversion of lithium polysulfides and uniform deposition of Li_2S, thereby contributing to high sulfur utilization. Consequently, the Li-S batteries assembled with these self-supported cathodes achieved a high areal capacity of 10.5 mAh cm^{-2} at 2 mA cm^{-2}. This versatile strategy of fabricating electrodes with a high loading of powder-like active materials can be applied to various energy storage systems, such as alkali metal batteries,

promoting their practical application.

Introduction

Li-S batteries have been regarded as one of the most promising energy storage technologies, because of their high theoretical energy density and low cost.[1-5] However, the low practical energy density of Li-S batteries, which is a consequence of poor utilization and mass-loading of sulfur, has hampered their wide application.[6,7] Low sulfur utilization stems from several problems, such as the "shuttle effect", sluggish reaction kinetics of lithium polysulfides conversion, high overpotential for Li_2S nucleation and low conductivity of S and Li_2S.[8,9] As a solution, the design of new host materials with high performance and the development of convenient electrode fabrication methods have been strongly demanded.[10,11]

Two-dimensional (2D) materials have attracted enormous attention in recent decades because of their superior functionalities that are associated with their unique electronic, magnetic, optical and thermal properties.[12-16] Among them, unilamellar metal oxide nanosheets have offered promising prospects in Li-S batteries because of their acid/base surface character and abundant exposed active sites.[17-20] On the other hand, the extremely high aspect ratio of 2D materials often causes a serious drawback, namely, a slow ion diffusion rate across the layers of electrode materials made of stacked 2D nanosheets. Thus, significant efforts have been devoted to drilling of 2D nanosheets, namely the artificial fabrication of in-plane pores by chemical/thermal etching and templating methods.[21-24] However, in general, such pores are not uniform in size, shape and arrangement, disabling the transportation of a specific ion and blocking others by so-called size-sieving effects. In contrast, an intrinsic crystalline nanomesh structure is expected to be more efficient and attractive because it provides ion-permeable channels with well-defined sizes and shapes. In addition, there is no need for steps that consume time, energy and chemicals as exemplified by the complex template-removal process in the reported procedures.[25] Although a number of unilamellar metal oxides have been reported,[12-16] nanosheets with such a nanomesh structure are very rare. The exfoliated TaO_3 nanosheet is such a unique example having in-plane pores.[26] The TaO_3 nanomesh can be derived from its

precursory layered oxide, $RbTaO_3$, via soft-chemical exfoliation into colloidal single layers.[27,28] The obtained TaO_3 nanomesh possesses in-plane pores with an open gap of 0.1-0.2 nm, which allow the penetration of small ions such as Li^+, as we experimentally confirmed.[29] Moreover, its Lewis acid surface and polar Ta-O bonds will provide a high catalytic activity and suitable binding to polysulfides. Accordingly, we expect that the TaO_3 nanomesh may be effectively employed in Li-S batteries as a multifunctional host material, namely, an anchor of polysulfides and the catalyst, to enhance sulfur utilization (Scheme 1b). Despite these promising advantages, no such study on the TaO_3 nanomesh has been reported. One aspect to be improved for oxide nanosheets, including TaO_3, is their insulating nature. We have reported that the layer-by-layer hybridization of various oxide nanosheets with reduced graphene oxide (rGO) into a superlattice composite can overcome this problem.[30-43]

Electrode fabrication methods bring about a significant difference in shape, porosity, stability, wettability, electrolyte uptake and mass loading, all of which affect total battery performance, such as energy and power densities.[44] However, relevant studies are scarce in comparison with electrode material design. In most of the studies, thin-film electrodes with a low sulfur loading (1-2 mg cm^{-2}) are fabricated by blade coating to guarantee sufficient mass transfer, electrical conductivity and structural stability of these compact electrodes.[45,46] Although it is an efficient method for screening studies on materials, the low sulfur loading inevitably leads to a poor energy density when practically used, which will leave a large gap between the fundamental study and practical application.[47] As an alternative, self-supported electrodes are promising to efficiently increase sulfur loading by reducing the proportion of inactive materials such as current collectors and binders.[48-50] Monolith-type[51] and membrane-type[52] electrodes are two typical self-supported electrodes, and they are usually prepared by hydrothermal/solvothermal reactions and suction filtration, respectively. In contrast to facile blade coating, these two methods require more time and energy; moreover, these methods are only applicable to a limited number of materials. These limitations have hampered their wide application. On the other hand, the pelletizing method is promising as a facile, efficient and widely applicable technique to fabricate self-supported electrodes with various materials,

including powder-like materials.[53] Moreover, electrode properties, such as mass loading, porosity and contact resistance, can be controlled by adjusting pelletizing conditions, such as pressure and time. Accordingly, the pelletizing method is anticipated to show great promise to fabricate electrodes for Li-S batteries as well as other batteries. However, related studies are still scarce.

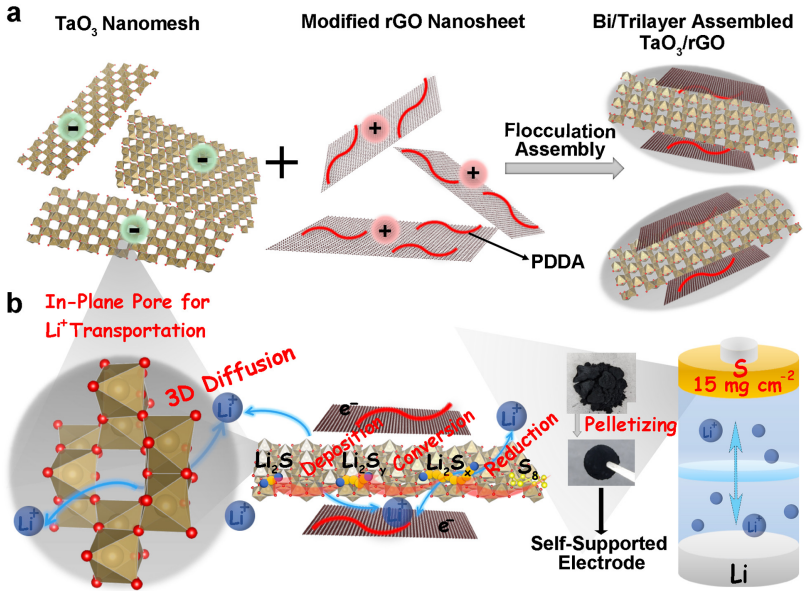

Scheme 1 Schematic illustration of the (a) pairwise/sandwich-like assembly of the TaO_3 nanomesh and rGO and (b) fabrication of the self-supported cathode based on the pairwise/sandwich-like assembly of TaO_3/rGO and its application in a lithium-sulfur battery.

Herein, we designed a unique material consisting of pairwise/sandwich-like assembly of TaO_3/rGO and constructed a self-supported cathode for Li-S batteries by the pelletizing method (Scheme 1). The unique nanomesh structure of TaO_3 was characterized by in-plane and powder X-ray diffraction (XRD) analysis and high angle angular dark field-scanning transmission electron microscopy (HAADF-STEM) clearly revealed the unique nanomesh structure of TaO_3. Li^+ penetration through the channels was demonstrated by density-functional theoretical (DFT) calculations as well as electrochemical experiments. The TaO_3 nanomesh with crystalline in-plane open pores (0.1-0.2 nm), polar Ta-O bonds, Lewis acid surfaces and abundant exposed active sites could accelerate Li^+ transfer, suppress the "shuttle effect", and promote the

conversion of lithium polysulfides and nucleation of Li_2S. Furthermore, the TaO_3 nanomesh was intimately combined with rGO, maximizing these advantages through improving electrical conductivity. Benefiting from the 2D morphology, the hetero-assembled material of TaO_3/rGO could be facilely pelletized into a self-supported cathode with a high sulfur-loading of 15 mg cm^{-2}, and achieved a high areal capacity of 10.5 mAh cm^{-2} at 2 mA cm^{-2}.

Results and discussion

Colloidal TaO_3 nanomeshes were derived from the parental layered material of $RbTaO_3$ via its soft-chemical delamination into single layers. XRD patterns of $RbTaO_3$ and its acid-exchanged form, $HTaO_3 \cdot 1.3H_2O$, can be indexed in terms of monoclinic structures, agreeing with the reported results[27] (Fig. S1). As shown in Fig. S2 and S3, these materials were composed of plate-like microcrystals. Shaking $HTaO_3 \cdot 1.3H_2O$ in a TBAOH solution for 10 days produced a colloidal suspension with an opalescent appearance (Fig. S4), indicating successful delamination. Atomic force microscopy (AFM) analysis was performed after drying a diluted suspension on an Si substrate. We observed 2D sheets with a lateral size of submicrometers and a thickness of ~1 nm (Fig. 1a), confirming their unilamellar structure. The in-plane XRD data of their monolayer film deposited on an Si wafer exhibited sharp diffraction peaks, indicating a highly crystalline nature (Fig. 1b). The peaks can be indexed to a face-centered rectangular lattice with refined unit cell dimensions of a = 0.9607 nm and b = 0.8479 nm. These values are very close to the in-plane lattice parameters of the parent material ($RbTaO_3$), indicating that the host layer architecture is preserved after exfoliation into nanosheets.

The structure of the TaO_3 nanomesh was further examined by HAADF-STEM. As shown in a ball-and-stick model of the TaO_3 host layer, each Ta atom is coordinated with six O atoms and the resulting octahedra are joined into a 2D sheet having two kinds of in-plane-holes to form a regular mesh structure (Fig. S5a). These in-plane-holes are more clearly recognized in the Ta atom pattern (Fig. S5c). One is marked by the rhombus (A), and the other is by the rhomboid with a pair of parallel red lines connected with a pair of parallel yellow lines (B). These holes correspond to the designation in the inset of Fig. 1b. A HAADF-STEM image of an exfoliated

TaO_3 nanosheet is shown in Fig. 1c. Because of the Z-contrast of the HAADF images, only the positions of the heavy Ta atoms can be identified to highlight the nanomesh structure, which is consistent with the atomic model (Fig. S5c) and the simulated HAADF image (Fig. 1d). The fast Fourier transform (FFT) pattern of this image is also compatible with the crystalline mesh structure (Fig. 1e). Accordingly, the obtained 2D sheet should have open channels as indicated by A and B (the inset of Fig. 1b and S5). The distances of orthogonally facing two oxygen atoms in the illustration are estimated as 0.39 nm and 0.46 nm (Fig. S5b), respectively, based on crystallographic data for the parent $RbTaO_3$. Note that there are displacements of the atoms along the sheet normal, making such interatomic distances appear shorter in the top view representation. Because the oxygen ionic radius is ~0.14 nm, the channels A and B have net open gaps of 0.11 nm and 0.18 nm, respectively, which appear to be large enough to allow penetration of Li^+ or some other metal ions for batteries.

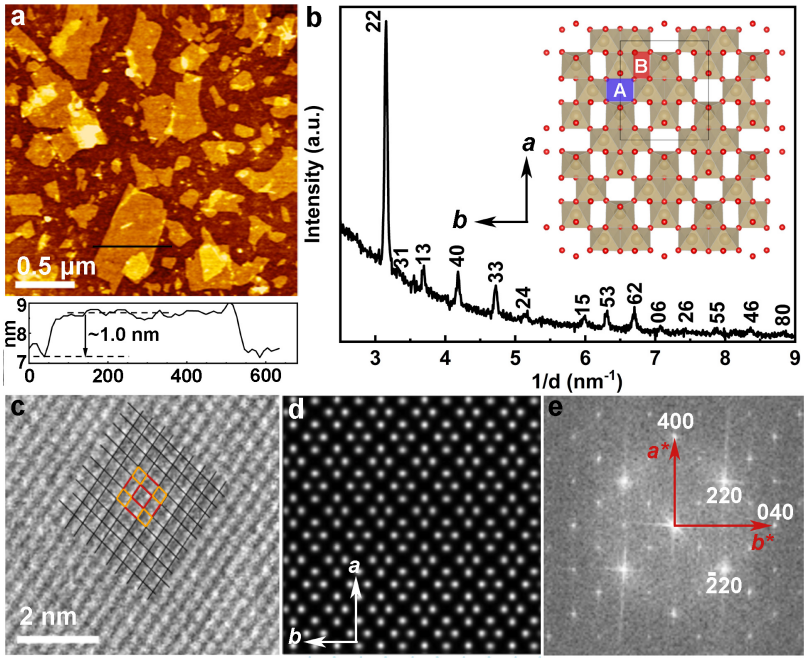

Fig. 1 (a) AFM image and height profile of the TaO_3 nanomeshes. (b) In-plane XRD pattern of a monolayer film of TaO_3 nanomeshes (inset: top-view of the TaO_3 layer[54]). (c) HAADF-STEM image of the TaO_3 nanomesh. (d) Simulated HAADF image of Ta atom positions in the TaO_3 layer. (e) FFT pattern of the HAADF-STEM image of the TaO_3 nanomesh in (c).

To examine the penetration possibility of metal ions such as Li^+, energy barriers of each channel were estimated by the nudged elastic band (NEB) method[55] based on the DFT calculations using the Vienna ab initio simulation package (VASP)[56] combined with the VTST code.[57] Fig. 2a-c show minimum energy paths (MEPs) by the NEB calculations for Li^+ ion penetration through A or B channels, and the energy barriers of each MEP are plotted in Fig. 2d. It should be noted that a TaO_3 slab-supercell model with surface protons was employed for establishing a charge neutral state of the nanomesh (Fig. S6) and two penetration paths for the B channel (as shown in Fig. 2b and c) were yielded due to the surface-proton configuration. As shown in Fig. 2d, the energy barrier for the A channel penetration is estimated to be nearly zero, while that for the B channel is rather large, ~1.5 eV. These evaluations suggest that the Li^+ ion is most likely to pass through the TaO_3 nanomesh via the A channel at room temperature, and this is consistent with our previous result.[29] The energy barriers for penetration of Na^+, K^+ and Mg^{2+} were also examined (Fig. S7), giving a lower barrier for the A channel in all the cases. The calculations indicate the easier penetration of the A channel than the B channel and the order of the ion penetration possibilities is, roughly, Li^+ (most penetrative) > Mg^{2+} > Na^+ >> K^+ (less penetrative), being compatible with an intuitive picture of "a smaller ion penetrates easier".[58] It is noteworthy that barrier heights of ~1 eV suggests a penetration wait time in the order of 10 h at room temperature from a simple rate constant analysis based on the harmonic transition state theory.[59] Thus we could conclude that it is hard for Na^+ (>2 eV) and K^+ (>8 eV) to penetrate both A and B channels. In contrast, Li^+ and Mg^{2+} can pass through the TaO_3 nanomesh along the A channel because almost zero barrier energies are expected. TaO_3 nanomeshes can provide channels for Li^+ and Mg^{2+} to promote diffusion especially in the vertical direction of the nanosheets, expecting the potential application opportunities of the TaO_3 nanomesh in Li^+ and Mg^{2+}-based metal ion batteries.

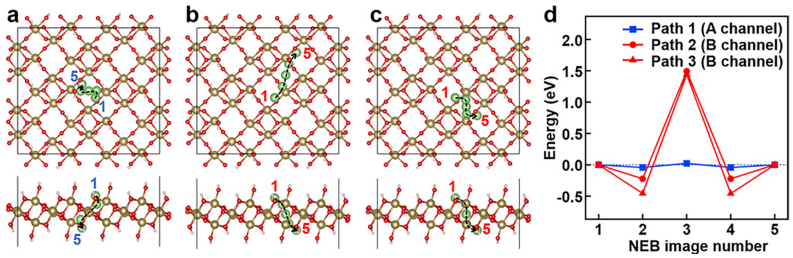

Fig. 2 Theoretical simulation results of Li^+ penetration through TaO_3 nanomesh. MEP images for (a) penetration path 1 (A channel), (b) path 2 (B channel) and (c) path 3 (B channel). (d) NEB relative energies for each MEP. In the initial (1st) and final (5th) images, Li^+ ions are located at metastable positions at the front and back side of the TaO_3 nanomesh. Each third image refers to a Li^+ ion just-in-the hole (bottleneck) structure yielding a penetration barrier energy.

Apart from the TaO_3 nanomesh, we prepared rGO according to the standard procedure. The modified Hummers' method was applied to synthesize graphite oxide (Fig. S8), which was delaminated by ultrasonication, modified with polycation, PDDA, and finally reduced with hydrazine.[60,61] This PDDA-modified rGO sample had a lateral size of several micrometers and a thickness of ~1.5 nm (Fig. S9). The zeta potential verifies that its surface charge changed from negative to positive through the modification with PDDA and the reduction, whereas the surface charge of the TaO_3 nanomesh was negative (Fig. S10).

To combine these 2D materials, namely, the TaO_3 nanomesh and PDDA-modified rGO, their suspensions were dropwise added to water at a specific ratio and the obtained composite is named as S-TaO_3/rGO (Scheme 1a) where "S" denotes self-assembled.[62-64] As a control, a composite named R-TaO_3/rGO ("R" denotes random) was prepared by adding suspensions of the negatively charged TaO_3 nanomesh and unmodified rGO into a PDDA solution. In addition, as a reference, self-restacked samples of the TaO_3 nanomesh and rGO were prepared by flocculation with PDDA solution followed by freeze-drying. Fig. 3 shows powder XRD data of these samples. The freeze-dried sample of the TaO_3 nanomesh showed strong peaks at 4.7° and 9.9°, which are attributable to the basal diffraction series from the restacked structure of the TaO_3 nanomesh, accommodating TBA^+ in the intersheet gallery (d = 1.90 nm). On the other

hand, the peaks at 14.3°, 28.4°, 33.3°, 37.7° and 43.0° can be indexed to the in-plane diffraction of the 110, 220, 130, 400 and 040 crystal planes of the face-centered rectangular unit cell (a = 0.96 nm, b = 0.85 nm). The freeze-dried sample of rGO was rather featureless, due to the small scattering factor of carbon. The material (S-TaO_3/rGO) obtained via the electrostatic assembly of the TaO_3 nanomesh and PDDA-modified rGO showed a series of in-plane reflections from TaO_3. No peak from rGO was detected, which should be due to the same reason above. The material showed an enhanced background toward small angles, which is superimposed by a characteristic wavy profile with humps at approximately 7° and 12° as indicated by arrows. The feature in this small angular range should be associated with the stacking structure of the 2D sheets, namely, how the TaO_3 and rGO are organized.

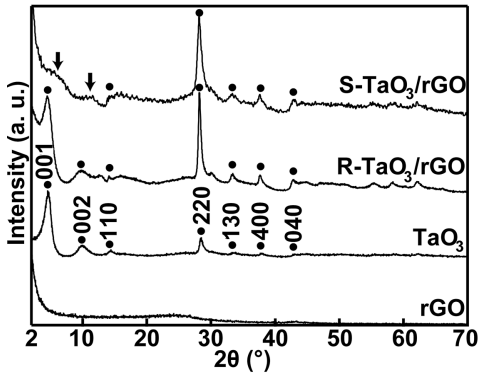

Fig. 3 Powder XRD patterns of the restacked PDDA-modified rGO, restacked TaO_3 nanomesh, R-TaO_3/rGO and S-TaO_3/rGO.

To gain insight into the stacking structure of the samples, we simulated the XRD profile based on Debye equation, the calculation details of which are given in the Experimental section. Fig. 4a depicts the calculated patterns of the individual TaO_3 nanomesh and rGO. The intensity steeply and monotonously increases with decreasing the 2θ angle. When these two sheets are paired with a separation of 1.5 nm, as illustrated in the model (Fig. S11a), the wavy profile with the gradually enhancing background (red line in Fig. 4b) reasonably reproduces the experimental pattern (Fig. 3, S-TaO_3/rGO). On the other hand, repeating this paired assembly (Fig. S11b) brings about the evolution of diffraction peaks together with small ripples

associated with the Laue interference function (blue line in Fig. 4b). These calculation results strongly suggest that the structure of the product obtained with the TaO_3 nanomesh and PDDA-modified rGO is close to their paired assembly. From a viewpoint of the chemical structure, it may be more reasonable to assume a sandwich-like architecture of rGO/TaO_3/rGO where rGO on one side is half of TaO_3 in the paired assembly (Fig. S11c). In practice, this rGO/TaO_3/rGO unit shows a very similar profile to that of the TaO_3/rGO pair as well as the experimentally observed data for S-TaO_3/rGO (Fig. 4c). TEM analysis provides a straightforward support for this unique sandwich-like structure, showing three parallel fringes with a distance of 1.5 nm (Fig. 4d, inset). Another composite of R-TaO_3/rGO prepared by mixing suspensions of the TaO_3 nanomesh and rGO in a PDDA solution showed a profile similar to that of S-TaO_3/rGO obtained by self-assembly, except for rather strong basal peaks at 4.5° and 9.8° (Fig. 3). These peaks may be identified as a self-restacked structure of PDDA/TaO_3. These results indicate that R-TaO_3/rGO is rather heterogeneous and is composed of the pairwise or sandwich-like assembly of S-TaO_3/rGO and self-restacked TaO_3 (and probably rGO). The segregative restacking may be reasonable, considering the mixing mode where two suspensions of the negatively charged TaO_3 nanomesh and rGO were simultaneously added into the polycation solution.

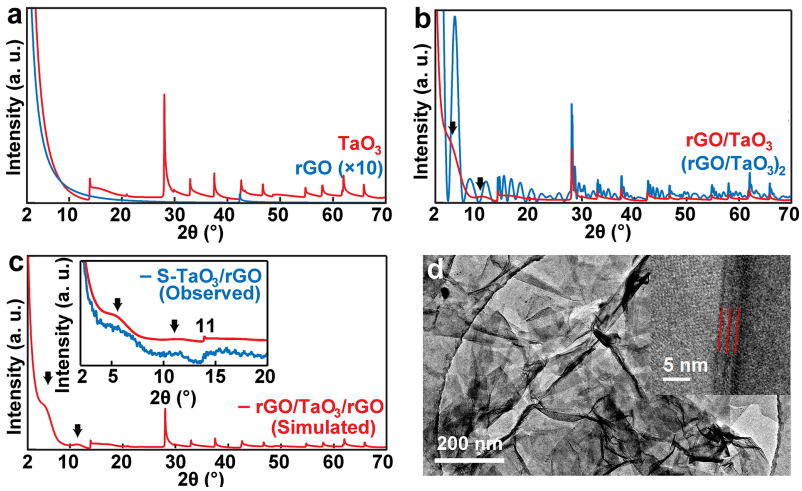

Fig. 4 Simulated XRD patterns of (a) single-layer TaO_3 and single-layer rGO, (b) single-unit of rGO/TaO_3 and double-unit rGO/TaO_3/rGO/TaO_3 and (c) sandwich-like architecture of rGO/TaO_3/rGO (inset: comparison with the observed XRD pattern of S-TaO_3/rGO in a low

angular region. The simulated one is plotted with some offset for clarity). (d) TEM image of S-TaO_3/rGO (inset: a high-resolution TEM image of the cross-section of the S-TaO_3/rGO sandwiched structure).

The TEM image of the self-assembled product of S-TaO_3/rGO displays a lath-like morphology with high transparency, indicating its ultrathin structure (Fig. 4d). The scanning electron microscopy (SEM) images reveal a loosely interconnected microstructure with a lateral size of several micrometers (Fig. S12), which will provide an electron conductive framework and electrolyte permeation path that contribute to the low ohmic and diffusion resistances. The uniform distribution of C, O and Ta was verified by energy-dispersive X-ray spectroscopy (EDS), indicating high homogeneity (Fig. S13). The sample underwent dehydration up to 200 °C, as revealed by thermogravimetric and differential thermal analysis (TG-DTA) (Fig. S14). The weight loss from 200 °C to 450 °C can be ascribed to the phase transition of TaO_3 to Ta_2O_5 and combustion of rGO. On the basis of the TG data, the mass ratio of TaO_3 to rGO is estimated to be ~4.3, which is close to the mass ratio (4.8) for preparation. Neglecting PDDA in the TG calculation may be responsible for the small difference between the TG calculation and preparation. All these results support the formation of the pairwise/sandwich-like assembly of the TaO_3 nanomesh with rGO through the present process involving flocculation via electrostatic self-assembly, suppressing their self-restacking.

The nanostructure/morphology of powder materials influences the structural adhesion effect of the pelletizing approach for fabricating self-supported electrodes. Thus, powder materials with various morphology, such as 1D carbon nanotubes (CNTs), 2D rGO and 3D activated carbon (Fig. S15), were chosen as model samples to explore structural adhesion behaviour. As illustrated in Fig. S16a and b, 1D CNTs failed to form a self-supported electrode at a pressure of 2 MPa and could be shaped into a brittle entity by applying a pressure of 14 MPa. A higher pressure of 28 MPa led to strong adhesion between the CNTs and mold substrate, and the electrode was cracked when being separated (Fig. S16c). The 3D activated carbon hardly formed a self-supported agglomerate at all the pressures (Fig. S16g-i). Small pieces were

obtained at high pressure, leaving residual fragments, which indicates that a higher pressure may be needed to obtain self-supported electrodes with activated carbon. In contrast, an intact rGO self-supported electrode was easily obtained at pressures of 2, 14 and 28 MPa (Fig. S16d-f). This wide pressure range for pelletizing demonstrates the high structural adhesion behaviour of rGO. The thickness of pelletized electrodes could be controlled by the pressure (Fig. S17), suggesting that the electrode performance can be optimized by the pelletizing parameter. The self-supported electrodes maintained the original intact disk shape with large variability in their thickness, indicating that these electrodes may tolerate a large volume change during charge/discharge processes, and thus, they may contribute to an excellent stability during long-term cycles. These findings suggest a strong structural adhesion characteristic of 2D materials, due to their high aspect ratio and ability to be readily stacked into a stable self-supported film, yielding remarkable benefits for facile electrode fabrication by pelletizing. The optimized pressure of 2 MPa was applied to preserve porosity for electrolyte permeability and guarantee the structural strength of the electrode for battery assembly, simultaneously. As a result, the S-TaO_3/rGO constructed with 2D blocks of monolayer rGO and the TaO_3 nanomesh was easily pelletized into self-supported electrodes (Fig. 5a). Self-supported electrodes based on rGO, R-TaO_3/rGO and S-TaO_3/rGO were fabricated by pelletizing to examine the catalytic activity to the lithium polysulfide conversion reaction and Li_2S nucleation process in Li_2S_6 symmetric batteries and Li_2S_8 batteries. The catalytic activity of rGO, R-TaO_3/rGO and S-TaO_3/rGO in regard to the conversion of lithium polysulfides was studied by cyclic voltammetry (CV) with Li_2S_6 symmetric batteries. The CV curve of rGO showed two pairs of redox peaks with oxidation peaks at 0.14 V and 0.71 V and reduction peaks at −0.18 V and −0.64 V, respectively, suggesting a two-step reaction on rGO (Fig. 5c). R-TaO_3/rGO showed a smaller peak separation of each redox peak than rGO, indicating that R-TaO_3/rGO has higher reversibility. This may be ascribed to the Lewis acidic surface of the TaO_3 nanomesh, which contributes to the high catalytic activity for the conversion of lithium polysulfides as a Lewis base.[65] On the other hand, the insulating nature of TaO_3 and its segregative restacking with rGO lead to a lower current response than that of rGO. The highest current response observed for S-TaO_3/rGO indicates

that it has the highest catalytic activity among the tested electrodes, verifying the advantages of the self-assembled pairwise or sandwich structure to maximize the number of exposed reaction sites. This feature is further supported by their electrochemical resistance, which was estimated by electrochemical impedance spectroscopy (EIS). As shown in Fig. S18, the impedance data were fitted with two compressed semicircles and one linear segment. These two semicircles correspond to the two-step reaction in the conversion process of long-chain lithium polysulfides to short-chain ones. The response from rGO, having the largest charge transfer resistance (R_{ct1} = 61.0 Ω, R_{ct2} = 15.4 Ω), suggests the slowest reaction kinetics for lithium polysulfide conversion. R-TaO_3/rGO showed a smaller charge transfer resistance (R_{ct1} = 34.0 Ω, R_{ct2} = 26.5 Ω) but a higher ohmic resistance (R_s = 12.5 Ω) than rGO (R_s = 5.7 Ω). The smallest charge transfer resistance (R_{ct1} = 3.8 Ω, R_{ct2} = 8.1 Ω) and ohmic resistance (R_s = 2.0 Ω) of S-TaO_3/rGO validate the highest electrical conductivity and fastest reaction kinetics, which may be ascribed to the molecular-level face-to-face contact between the TaO_3 nanomesh and rGO as well as the abundant exposed active sites.

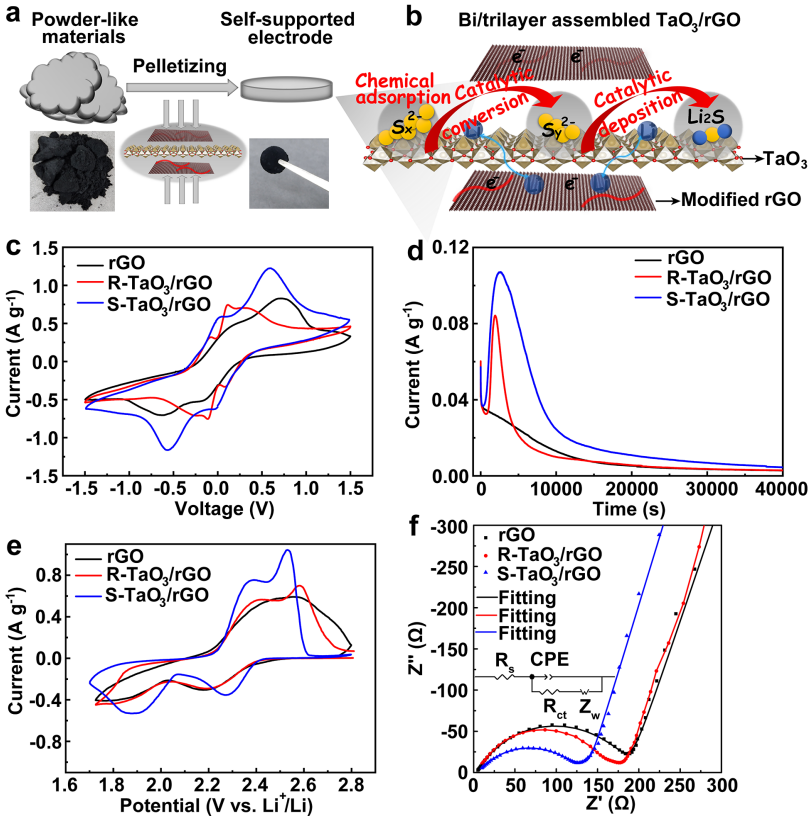

Fig. 5 (a) Schematic illustration showing the fabrication of self-supported electrodes based

on powder-like materials. (b) Schematic explanation for the effects of the pairwise or sandwich structure of TaO_3/rGO on improved sulfur utilization when used in Li-S batteries. (c) CV curves at a scan rate of 1 mV s^{-1} of the Li_2S_6 symmetric battery. (d) Current vs. time curves of a potentiostatic process at 2.05 V (vs. Li^+/Li) of the Li_2S_8 battery assembled with self-supported electrodes of rGO, R-TaO_3/rGO and S-TaO_3/rGO. (e) CV curves at 0.1 mV s^{-1} and (f) EIS curves of Li-S batteries assembled with self-supported sulfur-loaded cathodes of rGO, R-TaO_3/rGO and S-TaO_3/rGO (sulfur loading: 5 mg cm^{-2}).

The catalytic activity of rGO, R-TaO_3/rGO and S-TaO_3/rGO towards the Li_2S nucleation process was studied by potentiostatic amperometry on Li_2S_8 batteries (Fig. 5d). There are three regions in the curves of R-TaO_3/rGO and S-TaO_3/rGO and two regions for rGO. The first region, where the reduction current quickly decreased over time, corresponds to a liquid-liquid conversion process of soluble long-chain lithium polysulfides to short-chain ones. The second region where a peak appeared, specifically for R-TaO_3/rGO and S-TaO_3/rGO, is due to a liquid-solid nucleation process to generate solid Li_2S_2 or Li_2S.[66] The rise of the current for S-TaO_3/rGO started earlier than that for R-TaO_3/rGO, suggesting faster Li_2S deposition. Because the peak area is related to the amount of deposited Li_2S, the deposition capacity of S-TaO_3/rGO is much larger than that of R-TaO_3/rGO. The third region where the current decreased and leveled off corresponds to the conversion of soluble lithium polysulfides under diffusion-limited conditions. These current vs. time curves were fitted based on the mechanism and kinetics of Li_2S deposition on these samples (Fig. S19-S21). Based on the fitting results, the electrodeposition capacities of Li_2S of the R-TaO_3/rGO and S-TaO_3/rGO were 64 mAh g^{-1} and 184 mAh g^{-1}, respectively. The final products were characterized by Raman spectroscopy. The band at 373 cm^{-1} observed for R-TaO_3/rGO and S-TaO_3/rGO is diagnostic of Li_2S, verifying its nucleation on these materials (Fig. S22). The absence of such a Raman band for rGO, as well as a peak in the time dependence of the current, indicates that a higher overpotential is needed to drive the nucleation of Li_2S on rGO. These results indicate that the TaO_3 nanomesh can efficiently promote the electrochemical deposition of Li_2S, reducing the overpotential for its

nucleation. The electrochemical resistance of the samples after the potentiostatic process was monitored by EIS (Fig. S23), and an increase in the electrode resistance is expected due to the poor electrical conductivity of Li_2S. The large difference in the EIS curves between rGO (two compressed semicircles) and R-TaO_3/rGO and S-TaO_3/rGO (one compressed semicircle) may be mainly caused by the different overpotential for Li_2S nucleation. The Li_2S nucleation reaction is the main process on R-TaO_3/rGO and S-TaO_3/rGO in the Li_2S_8 electrolyte with tetraglyme. Because of the high overpotential for Li_2S nucleation, only the lithium polysulfide conversion reaction occurs on rGO, which is verified by the similar EIS curves of rGO in Li_2S_6 electrolyte with DOL/DME and Li_2S_8 electrolyte with tetraglyme. S-TaO_3/rGO maintained the smallest ohmic resistance (R_s = 5.7 Ω vs. 7.9 Ω for R-TaO_3/rGO, 9.5 Ω for rGO) even after the deposition of the largest amount of Li_2S. This superior performance may be due to the uniform distribution of Li_2S and intimate contact between Li_2S and S-TaO_3/rGO.

The effect of the pairwise or sandwich-like structure on the affinity to lithium polysulfides was studied by using Li_2S_6 as a representative example. Although a light-yellow colour of the Li_2S_6 solution remained when in contact with R-TaO_3/rGO, the solution became colourless with S-TaO_3/rGO, demonstrating the excellent affinity and adsorption by S-TaO_3/rGO (Fig. S24). The high adsorption capacity benefits from the pairwise or sandwich structure to maximize the exposed adsorption sites of the polar Ta-O bonds, which have excellent affinity for lithium polysulfides. Accordingly, it is expected that S-TaO_3/rGO blocks lithium polysulfides within the electrodes to reduce the crossover of lithium polysulfides and effectively overcome the "shuttle effect". All these results indicate that S-TaO_3/rGO demonstrates desirable confinement of lithium polysulfides, high catalytic activity for lithium polysulfides and effective nucleation of Li_2S, all of which will yield high electrochemical performance and largely enhanced sulfur utilization (Fig. 5b).

Self-supported sulfur-loaded cathodes based on rGO, R-TaO_3/rGO and S-TaO_3/rGO were fabricated by the impregnation method, wherein the pelletized self-supported electrode was immersed into the solution of sulfur in CS_2, to explore their application in Li-S batteries. Different from conventional film cathodes, these self-supported sulfur-loaded cathodes do not

contain binders or current collectors, thereby increasing active material content and sulfur loading (Fig. S25). This will eventually lead to Li-S batteries with a high areal capacity and energy density. The weight content of sulfur in these cathodes was controlled at around 50%. Their electrochemical performance was first examined by CV. The rGO cathode showed two reduction peaks at 2.17 V and 1.81 V and one broad oxidation peak at ~2.6 V (Fig. 5e). The R-TaO_3/rGO cathode showed two reduction peaks similar to those of rGO and two oxidation peaks at 2.39 V and 2.56 V. These two obvious oxidation peaks had a higher current than rGO, suggesting that R-TaO_3/rGO has higher electrochemical activity than rGO, which may result from the higher catalytic activity of TaO_3. The S-TaO_3/rGO cathode displayed two pairs of redox peaks, wherein the reduction peaks at 2.26 V and 1.87 V are ascribed to the conversion of sulfur to lithium polysulfides with long chains, then to those with short chains, and eventually to Li_2S. The reverse reaction took place during the reversed potential scan. The S-TaO_3/rGO cathode exhibited a much higher peak current and smaller separation of the peak potentials than R-TaO_3/rGO, demonstrating its superior activity and reversibility.

A fast mass transfer of Li^+ will enhance the rate performance of Li-S batteries to achieve a fast charge/discharge process, which is especially crucial for cathodes with high sulfur loading. Thus, the Li^+ transfer capacity in these cathodes was evaluated by CV at different scan rates (Fig. S26, S28 and S30). All samples showed an approximately linear relationship between the peak current (I_p) and the square root of the scan rate ($v^{1/2}$), indicating a diffusion-controlled process (Fig. S27, S29 and S31). Namely, the diffusion coefficient of Li^+ is proportional to the slope of the I_p vs. $v^{1/2}$ curve, indicating the mass transfer capacity. The S-TaO_3/rGO cathode showed the largest slope among the examined samples, indicating the highest mass transfer rate. Together with DFT calculations on Li^+ penetration, these results validate the efficiency of the intrinsic crystalline in-plane pores in the TaO_3 nanomesh as the channels for generating a 3D transfer mode and decreasing the Li^+ diffusion distance, leading to a superior rate performance.

A polysulfide permeability test was also performed to evaluate the size-sieving capability of the TaO_3 nanomesh overcoming the “shuttle effect”. The original colourless solvent in the right tube turned light yellow after 0.5 h (Fig. S32b), indicating the crossover of polysulfides through

the Celgard separator. The colour became darker and darker over time, as a result of an increasingly more serious crossover of polysulfides (Fig. S32a-d). In contrast, polysulfide crossover was substantially suppressed by modifying the Celgard separator with TaO_3 nanomesh, indicating that the TaO_3 nanomesh can efficiently confine polysulfides (Fig. S32e-h). This result agrees well with the geometrical considerations based on the crystallographic data that the polysulfides are too large to pass through the channels of the TaO_3 nanomesh. These results reveal that S-TaO_3/rGO exerts superior performance, allowing the penetration of Li^+ while blocking polysulfides. Recently, similar behaviour has been reported in $Ti_{0.87}O_2$ nanosheets.[67] The larger number of the open channels in the TaO_3 nanomesh can provide a more efficient penetration path for Li^+ compared with $Ti_{0.87}O_2$, where Ti site vacancies work as a migration route.

The electrochemical resistance of these cathodes was estimated by EIS. All samples showed a similar response profile: a semicircle in the high-frequency region corresponding to the charge transfer resistance and a linear segment in the low-frequency region (Fig. 5f). The S-TaO_3/rGO cathode showed the smallest charge transfer resistance (R_{ct} = 119.5 Ω vs. 159.7 Ω for R-TaO_3/rGO and 188.3 Ω for rGO), indicating the highest catalytic activity. These results demonstrate the excellent electrochemical performance of S-TaO_3/rGO, verifying the advantages of the pairwise/sandwich structure and promoting its application in Li-S batteries.

Charge/discharge tests were performed with Li-S batteries assembled with the self-supported cathodes with a high sulfur loading to demonstrate their practical application. Compared with sulfur-loaded host cathodes (Fig. 6a and b), unloaded host electrodes contributed a negligible capacity to Li-S batteries (Fig. S33), identifying that sulfur is the active material. Upon charging/discharging at 2 mA cm^{-2} with a sulfur loading of 5 mg cm^{-2}, the S-TaO_3/rGO cathode delivered a discharge capacity of 1139 mAh g^{-1}, while the rGO cathode and R-TaO_3/rGO cathode displayed capacities of 584 mAh g^{-1} and 871 mAh g^{-1}, respectively (Fig. 6a). All cathodes showed two couples of charge/discharge plateaus; the charge/discharge plateaus at the higher potential may correspond to the conversion between sulfur and long-chain lithium polysulfides, while those at the lower potential correspond to the conversion between

long-chain lithium polysulfides and short-chain ones all the way to Li_2S. The corresponding capacities of these two processes in the discharging process are marked as Q_1 and Q_2 (Fig. 6a). The potential difference (ΔE) between the charge and discharge plateaus indicates battery polarization. A large battery polarization will reduce sulfur utilization. The S-TaO_3/rGO cathode showed a reduced polarization potential (Fig. 6c), contributing to a high battery capacity. The shorter plateau at the higher potential compared with that at the lower potential in the discharging process indicates $Q_1 < Q_2$, suggesting a smaller capacity contribution of the conversion process from sulfur to long-chain lithium polysulfides (Fig. 6d). The S-TaO_3/rGO cathode showed a much larger Q_2 and a slightly larger or even similar Q_1 to that of rGO and R-TaO_3/rGO, indicating efficient conversion from long-chain lithium polysulfides to short-chain ones and eventually to nucleated Li_2S.

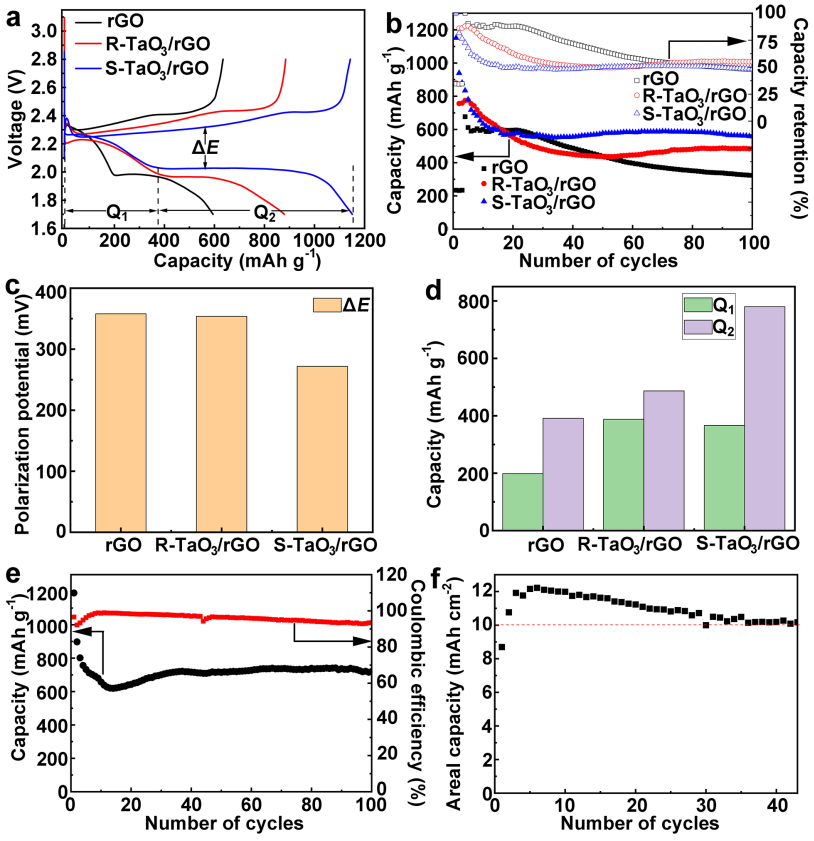

Fig. 6 (a) Galvanostatic charge/discharge curves at 2 mA cm^{-2} and (b) cycle performance of Li-S batteries assembled with self-supported cathodes with a sulfur-loading of 5 mg cm^{-2}. (c) Potential difference ΔE and (d) capacities Q_1 and Q_2 observed in (a). Cycle performance of Li-

S batteries assembled with self-supported S-TaO_3/rGO cathodes with a sulfur loading of (e) 10 mg cm^{-2} and (f) 15 mg cm^{-2} upon charging/discharging at (e) 1 mA cm^{-2} and (f) 2 mA cm^{-2}.

The stability of these cathodes was examined by repeating the charge/discharge cycle. As shown in Fig. 6b, the higher initial discharge capacity of S-TaO_3/rGO than R-TaO_3/rGO and rGO means the higher sulfur utilization in S-TaO_3/rGO. The huge quantity of underutilized sulfur in R-TaO_3/rGO and rGO offsets their capacity decrease, resulting in a comparable discharge capacity of R-TaO_3/rGO to S-TaO_3/rGO between cycles 10 and 20 and an even higher discharge capacity of rGO than R-TaO_3/rGO between cycles 20 and 50. Nevertheless, the discharge capacity of the S-TaO_3/rGO cell gradually decreased from 1139 mAh g^{-1} to 559 mAh g^{-1} in the first ~10 cycles, and then the capacity was well maintained over 100 cycles. The cells based on R-TaO_3/rGO and rGO also showed decreasing discharge capacities during 100 cycles from 879 mAh g^{-1} to 484 mAh g^{-1} and from 593 mAh g^{-1} to 326 mAh g^{-1}, respectively. All the samples exhibited a similar capacity retention around 50% after 100 cycles. The observed capacity decrease in the first 10 cycles may be because the lithium polysulfides formed during the charge/discharge cycle were gradually escaped from the cathodes. However, the largest capacity was preserved owing to the effective confinement of polysulfides as well as high catalytic activity for Li_2S deposition in the S-TaO_3/rGO. The S-TaO_3/rGO cathodes with higher sulfur loading were further explored to develop their practical application. With a sulfur-loading of 10 mg cm^{-2}, the S-TaO_3/rGO cathode delivered an initial discharge capacity of 1190 mAh g^{-1} at 1 mA cm^{-2}, which decreased to 741 mAh g^{-1} after 100 cycles (Fig. 6e). With a sulfur loading of 15 mg cm^{-2}, a lower capacity was observed in the initial several cycles, which may be attributed to the poor distribution of sulfur due to high sulfur-loading as well as the thick cathode. It recovered soon after improvement by an activation process (Fig. 6f). A high areal capacity of 12.2 mAh cm^{-2} was attained at 2 mA cm^{-2}, and 10.5 mAh cm^{-2} and above was retained after 40 cycles, corresponding to a capacity of 674 mAh g^{-1}. Compared with the reported results, the areal capacity and sulfur loading are significantly enhanced by S-TaO_3/rGO in this study (Fig. S34). These results demonstrate that S-TaO_3/rGO achieves a high capacity

with a high sulfur loading, significantly improving sulfur utilization and leading to a high practical energy density.

Conclusions

We reported a strategy to develop high-performance Li-S batteries using the unique 2D material with open channels. A TaO_3 nanomesh was self-assembled with rGO into the pairwise/sandwich-like assembly, which was pelletized into self-supported electrodes with high sulfur loading. The pairwise or sandwich-like composite of S-TaO_3/rGO not only efficiently catalyzed the conversion to lithium polysulfides and Li_2S nucleation, but also promoted Li^+ transfer and polysulfide confinement. These multifunctionalities were realized by maximizing the synergistic effects derived from the TaO_3 nanomesh with its polar Ta-O bonds, Lewis acid surfaces and intrinsic in-plane pores with size between Li^+ and polysulfides, and rGO with high electrical conductivity. Owing to the sticking property of the composite featuring a 2D morphology, the self-supported cathode with high sulfur loading could be easily fabricated at room temperature by the pelletizing-impregnation method to enhance the practical energy density of Li-S batteries. As a result, a Li-S battery employing the designed self-supported S-TaO_3/rGO cathode achieved an areal capacity as high as 10.5 mAh cm^{-2} at 2 mA cm^{-2} after 40 cycles. This work has verified a new process to develop self-supported cathodes with a high sulfur loading, accelerating the application and commercialization of Li-S batteries. Furthermore, this approach can be applied to other energy storage systems, such as Li-ion and Mg-ion batteries.

Author Contributions

Chenhui Wang: methodology, validation, investigation, writing - original draft, visualization. Nobuyuki Sakai: writing - review & editing. Yasuo Ebina: investigation. Takayuki Kikuchi: investigation. Shigeru Suehara: validation. Daiming Tang: investigation. Renzhi Ma: writing - review & editing. Takayoshi Sasaki: conceptualization, supervision, writing - review & editing.

Conflicts of interest

There are no conflicts to declare.

Acknowledgements

The authors greatly acknowledge the support of the World Premier International Research Center Initiative on Materials Nanoarchitectonics (WPI-MANA), Ministry of Education, Culture, Sports, Science and Technology (MEXT), Japan, CREST of the Japan Science and Technology Agency (JST) (Grant No. JPMJCR17N1), and Japan Society for the Promotion of Science (JSPS) (Grant No. P21036). All the DFT and XRD simulations were conducted with the supercomputer at the Numerical Materials Simulator Station in NIMS. The Raman spectra were measured at the Namiki Foundry in NIMS (938, 19-275). The in-plane XRD measurements were performed under the approval of the Photon Factory Program Advisory Committee (Proposal No. 2020G503).

References

1. A. Manthiram, Y. Fu, S. H. Chung, C. Zu and Y. S. Su, *Chem. Rev.*, 2014, **114**, 11751-11787.
2. Y. X. Yin, S. Xin, Y. G. Guo and L. J. Wan, *Angew. Chem. Int. Ed.*, 2013, **52**, 13186-13200.
3. A. Manthiram, S. H. Chung and C. Zu, *Adv. Mater.*, 2015, **27**, 1980-2006.
4. X. Shan, Y. Zhong, L. Zhang, Y. Zhang, X. Xia, X. Wang and J. Tu, *J. Phys. Chem. C*, 2021, **125**, 19060-19080.
5. X. Yan, L. Lin, Q. Chen, Q. Xie, B. Qu, L. Wang and D.-L. Peng, *Carbon Energy*, 2021, **3**, 303-329.
6. Y. Yang, G. Zheng and Y. Cui, *Chem. Soc. Rev.*, 2013, **42**, 3018-3032.
7. S. Evers and L. F. Nazar, *Acc. Chem. Res.*, 2013, **46**, 1135-1143.
8. S. Zhou, S. Yang, X. Ding, Y. Lai, H. Nie, Y. Zhang, D. Chan, H. Duan, S. Huang and Z. Yang, *ACS Nano*, 2020, **14**, 7538-7551.

9. X. Yang, X. Gao, Q. Sun, S. P. Jand, Y. Yu, Y. Zhao, X. Li, K. Adair, L. Y. Kuo, J. Rohrer, J. Liang, X. Lin, M. N. Banis, Y. Hu, H. Zhang, X. Li, R. Li, H. Zhang, P. Kaghazchi, T. K. Sham and X. Sun, *Adv. Mater.*, 2019, **31**, 1901220.
10. D. Lv, J. Zheng, Q. Li, X. Xie, S. Ferrara, Z. Nie, L. B. Mehdi, N. D. Browning, J.-G. Zhang, G. L. Graff, J. Liu and J. Xiao, *Adv. Energy Mater.*, 2015, **5**, 1402290.
11. C. Wang, Y. Li, F. Cao, Y. Zhang, X. Xia and L. Zhang, *ACS Appl. Mater. Interfaces*, 2022, **14**, 10457-10466.
12. R. Ma and T. Sasaki, *Adv. Mater.*, 2010, **22**, 5082-5104.
13. L. Wang and T. Sasaki, *Chem. Rev.*, 2014, **114**, 9455-9486.
14. S. Z. Butler, S. M. Hollen, L. Cao, Y. Cui, J. A. Gupta, H. R. Gutiérrez, T. F. Heinz, S. S. Hong, J. Huang, A. F. Ismach, E. Johnston-Halperin, M. Kuno, V. V. Plashnitsa, R. D. Robinson, R. S. Ruoff, S. Salahuddin, J. Shan, L. Shi, M. G. Spencer, M. Terrones, W. Windl and J. E. Goldberger, *ACS Nano*, 2013, **7**, 2898-2926.
15. V. Nicolosi, M. Chhowalla, M. G. Kanatzidis, M. S. Strano and J. N. Coleman, *Science*, 2013, **340**, 1226419.
16. R. Ma and T. Sasaki, *Acc. Chem. Res.*, 2015, **48**, 136-143.
17. T. Ali and C. Yan, *ChemSusChem*, 2020, **13**, 1447-1479.
18. C. Ye, D. Chao, J. Shan, H. Li, K. Davey and S.-Z. Qiao, *Matter*, 2020, **2**, 323-344.
19. Q. Shao, Z.-S. Wu and J. Chen, *Energy Storage Mater.*, 2019, **22**, 284-310.
20. S. B. Patil, H. J. Kim, H.-K. Lim, S. M. Oh, J. Kim, J. Shin, H. Kim, J. W. Choi and S.-J. Hwang, *ACS Energy Lett.*, 2018, **3**, 412-419.
21. J. L. Shi, C. Tang, H. J. Peng, L. Zhu, X. B. Cheng, J. Q. Huang, W. Zhu and Q. Zhang, *Small*, 2015, **11**, 5243-5252.
22. K. Adpakpang, S. M. Oh, D. A. Agyeman, X. Jin, N. Jarulertwathana, I. Y. Kim, T. Sarakonsri, Y.-M. Kang and S.-J. Hwang, *Adv. Funct. Mater.*, 2018, **28**, 1707106.
23. J. Bai, X. Zhong, S. Jiang, Y. Huang and X. Duan, *Nat. Nanotechnol.*, 2010, **5**, 190-194.
24. Y. Li, J. J. Gutiérrez Moreno, Z. Song, D. Liu, M. Wang, A. Ramiere, Z. Feng, Q. J. Niu, T. Sasaki and X. Cai, *ACS Appl. Mater. Interfaces*, 2022, **14**, 18513-18524.

25. T. Wang, Q. Zhang, J. Zhong, M. Chen, H. Deng, J. Cao, L. Wang, L. Peng, J. Zhu and B. Lu, *Adv. Energy Mater.*, 2021, **11**, 2100448.
26. M. Serafin and R. Hoppe, *Angew. Chem. Int. Ed.*, 1978, **17**, 354-355.
27. K. Fukuda, I. Nakai, Y. Ebina, R. Ma and T. Sasaki, *Inorg. Chem.*, 2007, **46**, 4787-4789.
28. J. Huang, R. Ma, Y. Ebina, K. Fukuda, K. Takada and T. Sasaki, *Chem. Mater.*, 2010, **22**, 2582-2587.
29. X. Xu, K. Takada, K. Fukuda, T. Ohnishi, K. Akatsuka, M. Osada, B. T. Hang, K. Kumagai, T. Sekiguchi and T. Sasaki, *Energy Environ. Sci.*, 2011, **4**, 3509-3512.
30. P. Xiong, R. Ma, G. Wang and T. Sasaki, *Energy Storage Mater.*, 2019, **19**, 281-298.
31. P. Xiong, B. Sun, N. Sakai, R. Ma, T. Sasaki, S. Wang, J. Zhang and G. Wang, *Adv. Mater.*, 2020, **32**, 1902654.
32. R. Ma, X. Liu, J. Liang, Y. Bando and T. Sasaki, *Adv. Mater.*, 2014, **26**, 4173-4178.
33. W. Ma, R. Ma, C. Wang, J. Liang, X. Liu, K. Zhou and T. Sasaki, *ACS Nano*, 2015, **9**, 1977-1984.
34. X. Cai, N. Sakai, T. C. Ozawa, A. Funatsu, R. Ma, Y. Ebina and T. Sasaki, *ACS Appl. Mater. Interfaces*, 2015, **7**, 11436-11443.
35. W. Ma, R. Ma, J. Wu, P. Sun, X. Liu, K. Zhou and T. Sasaki, *Nanoscale*, 2016, **8**, 10425-10432.
36. P. Xiong, R. Ma, N. Sakai and T. Sasaki, *ACS Nano*, 2018, **12**, 1768-1777.
37. X. Lu, N. Sakai, D. Tang, X. Li, T. Taniguchi, R. Ma and T. Sasaki, *ACS Appl. Mater. Interfaces*, 2020, **12**, 33083-33093.
38. P. Xiong, X. Zhang, H. Wan, S. Wang, Y. Zhao, J. Zhang, D. Zhou, W. Gao, R. Ma, T. Sasaki and G. Wang, *Nano Lett.*, 2019, **19**, 4518-4526.
39. P. Sun, Q. Chen, X. Li, H. Liu, K. Wang, M. Zhong, J. Wei, D. Wu, R. Ma, T. Sasaki and H. Zhu, *NPG Asia Mater.*, 2015, **7**, e162.
40. P. Sun, R. Ma, W. Ma, J. Wu, K. Wang, T. Sasaki and H. Zhu, *NPG Asia Mater.*, 2016, **8**, e259.
41. N. Sakai, K. Kamanaka and T. Sasaki, *J. Phys. Chem. C*, 2016, **120**, 23944-23950.

42. X. Cai, L. Yin, N. Sakai, D. Liu, C. Teng, Y. Ebina, R. Ma and T. Sasaki, *ACS Appl. Nano Mater.*, 2019, **2**, 6378-6386.

43. P. Xiong, X. Zhang, F. Zhang, D. Yi, J. Zhang, B. Sun, H. Tian, D. Shanmukaraj, T. Rojo, M. Armand, R. Ma, T. Sasaki and G. Wang, *ACS Nano*, 2018, **12**, 12337-12346.

44. Y. Yu, H. Zhang, X. Yang, J. Gou, X. Tong, X. Li and H. Zhang, *Energy Storage Mater.*, 2019, **19**, 88-93.

45. L. Fei, X. Li, W. Bi, Z. Zhuo, W. Wei, L. Sun, W. Lu, X. Wu, K. Xie, C. Wu, H. L. Chan and Y. Wang, *Adv. Mater.*, 2015, **27**, 5936-5942.

46. X. Liang, Y. Rangom, C. Y. Kwok, Q. Pang and L. F. Nazar, *Adv. Mater.*, 2017, **29**, 1603040.

47. M. A. Pope and I. A. Aksay, *Adv. Energy Mater.*, 2015, **5**, 1500124.

48. J. He, G. Hartmann, M. Lee, G. S. Hwang, Y. Chen and A. Manthiram, *Energy Environ. Sci.*, 2019, **12**, 344-350.

49. Z. Li, Q. He, X. Xu, Y. Zhao, X. Liu, C. Zhou, D. Ai, L. Xia and L. Mai, *Adv. Mater.*, 2018, **30**, 1804089.

50. Q. Xiao, J. Yang, X. Wang, Y. Deng, P. Han, N. Yuan, L. Zhang, M. Feng, C.-a. Wang and R. Liu, *Carbon Energy*, 2021, **3**, 271-302.

51. Z. Sun, J. Zhang, L. Yin, G. Hu, R. Fang, H. M. Cheng and F. Li, *Nat. Commun.*, 2017, **8**, 14627.

52. S. Luo, M. Yao, S. Lei, P. Yan, X. Wei, X. Wang, L. Liu and Z. Niu, *Nanoscale*, 2017, **9**, 4646-4651.

53. J.-Y. Hwang, S. Shin, C. S. Yoon and Y.-K. Sun, *ACS Energy Lett.*, 2019, **4**, 2787-2795.

54. K. Momma and F. Izumi, *J. Appl. Crystallogr.*, 2011, **44**, 1272-1276.

55. D. Sheppard, P. Xiao, W. Chemelewski, D. D. Johnson and G. Henkelman, *J. Chem. Phys.*, 2012, **136**, 074103.

56. G. Kresse and D. Joubert, *Phys. Rev. B*, 1999, **59**, 1758-1775.

57. https://theory.cm.utexas.edu/vtsttools/, Transition State Tools for VASP site.

58. R. D. Shannon, *Acta Crystallogr.*, 1976, **32**, 751-767.

59. D. S. Sholl and J. A. Steckel, in *Density Functional Theory: A Practical Introduction*, John Wiley & Sons, Inc., 2009, ch. 6, pp. 131-161, DOI: 10.1002/9780470447710.ch6.

60. C. Wang, N. Sakai, Y. Ebina, T. Kikuchi, M. R. Snowdon, D. Tang, R. Ma and T. Sasaki, *J. Mater. Chem. A*, 2021, **9**, 9952-9960.

61. S. Park, J. An, R. D. Piner, I. Jung, D. Yang, A. Velamakanni, S. T. Nguyen and R. S. Ruoff, *Chem. Mater.*, 2008, **20**, 6592-6594.

62. L. Li, R. Ma, Y. Ebina, K. Fukuda, K. Takada and T. Sasaki, *J. Am. Chem. Soc.*, 2007, **129**, 8000-8007.

63. X. Cai, T. C. Ozawa, A. Funatsu, R. Ma, Y. Ebina and T. Sasaki, *J. Am. Chem. Soc.*, 2015, **137**, 2844-2847.

64. R. Ma and T. Sasaki, *Annu. Rev. Mater. Res.*, 2015, **45**, 111-127.

65. D.-R. Deng, F. Xue, Y.-J. Jia, J.-C. Ye, C.-D. Bai, M.-S. Zheng and Q.-F. Dong, *ACS Nano*, 2017, **11**, 6031-6039.

66. F. Y. Fan, W. C. Carter and Y. M. Chiang, *Adv. Mater.*, 2015, **27**, 5203-5209.

67. P. Xiong, F. Zhang, X. Zhang, Y. Liu, Y. Wu, S. Wang, J. Safaei, B. Sun, R. Ma, Z. Liu, Y. Bando, T. Sasaki, X. Wang, J. Zhu and G. Wang, *Nat. Commun.*, 2021, **12**, 4184.